HHS Public Access

Author manuscript

Dev Neurosci. Author manuscript; available in PMC 2023 January 01.

Published in final edited form as:

Dev Neurosci. 2022 ; 44(4-5): 214–232. doi:10.1159/000521611.

Intrauterine growth restriction disrupts the postnatal critical period of synaptic plasticity in the mouse dorsal hippocampus in a model of hypertensive disease of pregnancy

Mark St. Pierre[1], **Neetika Rastogi**[2], **Ashley Brown**[3], **Pritika Parmar**[2], **Charles Lechner**[1], **Camille Fung**[3], **Raul Chavez-Valdez**[1,*]

[1]Division of Neonatal-Perinatal Medicine, Department of Pediatrics, Johns Hopkins School of Medicine. Baltimore, MD

[2]Department of Neurosciences, Johns Hopkins University Krieger School of Arts and Sciences, Baltimore, MD

[3]Division of Neonatology, Department of Pediatrics, University of Utah, Salt Lake City, UT.

Abstract

Introduction: Intrauterine growth restriction (IUGR) from hypertensive disease of pregnancy complicates up to 10% of all pregnancies. Significant hippocampal-dependent cognitive and memory impairments as well as neuropsychiatric disorders have been linked to IUGR. Because disturbance of hippocampal critical period (CPd) of synaptic plasticity leads to impairments similar to those described in IUGR human offspring, we hypothesized that IUGR would perturb the CPd of synaptic plasticity in the mouse hippocampus in our model.

Methods: IUGR was produced by a micro-osmotic pump infusion of the potent vasoconstrictor U-46619, a thromboxane A_2-agonist (TXA_2), at embryonic day (E) 12.5 in C57BL/6J mouse dams to precipitate hypertensive disease of pregnancy and IUGR. Sham-operated mice acted as controls. At P10, P18, and P40, we assessed astrogliosis using GFAP-IHC. In dorsal CA1 and CA3 subfields, we assessed the immunoreactivities (IR) (IF-IHC) to: i) parvalbumin (PV) and glutamate decarboxylase (GAD) 65/67, involved in CPd onset; ii) PSA-NCAM, that antagonizes CPd onset; iii) NPTX2, necessary for excitatory synapse formation and engagement of CPd;

[*]**Corresponding author:** Dr. Raul Chavez-Valdez. Associate Professor. Department of Pediatrics, Division of Neonatology, Johns Hopkins Hospital, 600 N. Wolfe Street, CMSC 6-104, Baltimore, MD 21287, USA. Telephone: (410) 955-7156, rchavez2@jhmi.edu.

AUTHOR CONTRIBUTIONS. All authors had full access to all the data in the study and take responsibility for the integrity of the data and the accuracy of the data analysis. Contributions: RC-V and CF in conception; RC-V, MSP and CF in design; all authors in acquisition of data; RC-V, MSP, NR, and CL in analysis, RC-V, MSP, NR, and CF in data interpretation, RC-V, MSP, NR, and CF in drafting of manuscript; and RC-V, and CF in funding acquisition. All authors have critically reviewed the final manuscript for important intellectual content and have given their final approval for publication.

STATEMENT OF ETHICS

We confirm that any aspect of the work covered in this manuscript involving experimental animals has been conducted with the ethical approval by the University of Utah Animal Care Committee (19–02001) and were carried out in accordance with the NIH Guide for the Care and Use of Laboratory Animals.

DISCLOSURE/CONFLICT OF INTEREST

We confirm that there are no known conflicts of interest associated with this publication and there has been no significant financial support for this work that could have influenced its outcome.

Supplementary material is available on line at Developmental Neuroscience

and iv) MBP and WFA, staining perineural nets (PNNs), marking CPd closure. ImageJ/Fiji and IMARIS were used for image processing and SPSS v24 for statistical analysis.

Results: Although PV^+ interneuron (IN) numbers and IR intensity were unchanged, development of $GAD65/67^+$ synaptic boutons was accelerated at P18 IUGR mice, and inversely correlated with decreased expression of PSA-NCAM in the CA of P18 IUGR mice at P18. NPTX2 $^+$ puncta and total volume were persistently decreased in the CA3 pyramidal and radiatum layers of IUGR mice from P18 to P40. At P40, axonal myelination (MBP^+) in CA3 of IUGR mice was decreased and correlated with NPTX2 deficits. Lastly, the volume and integrity of the PNNs in the dorsal CA was disrupted in IUGR mice at P40.

Discussion/Conclusion: IUGR disrupts the molecular and structural initiation, consolidation and closure of the CPd of synaptic plasticity in the mouse hippocampus in our model, which may explain the learning and memory deficits observed in juvenile IUGR mice and the cognitive disorders seen in human IUGR offspring. The mechanistic links warrant further investigation, to identify therapeutic targets to prevent neurodevelopmental deficits in patients affected by IUGR.

Keywords

interneurons; memory; neuropsychiatric disorders; synaptic plasticity

INTRODUCTION

Intrauterine growth restriction (IUGR) occurs when the fetus fails to attain expected growth based on genetic potential. IUGR is the most common early life stressor affecting up to 10% of all pregnancies [1]. Uteroplacental insufficiency secondary to hypertensive disease of pregnancy is the most common cause of IUGR in the developed world [2]. IUGR increases morbidity and mortality in neonates[3–5] by impairing cortical development [6–8], connectivity [9], cognition [10,11], and memory [12,13]. In the hippocampus, IUGR produces hypoplasia and reduced number and dendritic complexity of neurons [12–15]. IUGR models that produce a hypertensive-like phenotype in pregnancy mirror these human findings by replicating hippocampal hypoplasia [16] and hippocampal-dependent memory deficits,[17–19] which are common in neurodevelopmental disorders and psychopathologies [20,21]. However, the mechanisms underlying these structural and functional deficits need further investigation.

Postnatal critical periods (CPd) of synaptic plasticity are characterized by profound refinement and remodeling of brain circuits, with extensive neurite outgrowth, synaptic formation, and pruning to create mature networks sculpted by experience [22]. The CPd boundaries are determined by complex biochemical and structural events. Among them, decreased polysialylation of the neural cell adhesion molecule (PSA-NCAM) in the excitatory neuronal membranes, and advanced maturation of parvalbumin $(PV)^+$ interneurons (INs) resulting in GABAergic network development with increased number of glutamate decarboxylase (GAD) $^+$ synaptic boutons (also known as axonal terminals) open the CPd [22–27]. On the other hand, increased neuronal pentraxin 2 (NPTX2 or Narp) production by pyramidal cells, with later localization on GluA4 subunit of AMPA receptors onto PV^+ INs, allows development of excitatory synapses and consolidation of

the CPd [28,29]. Lastly, advanced myelination, and formation of perineural nets (PNNs) supporting NPTX2 proximity to PV^+ INs close this period [22,30–34]. Many of these events are common to the somatosensory cortex, the amygdala and the hippocampus [24,25,35–38]. However, these regional CPd progress sequentially, with somatosensory cortex and amygdala temporally preceding that of the hippocampus [35]. Dysregulation of the CPd temporal progression, which in rodent hippocampi is postulated to start between postnatal age (P)17-P21 and to close during late adolescence (>P30), [25,35,38–40] results in alterations in the excitatory/inhibitory (E/I) balance, which may contribute to neurodevelopmental disorders and psychopathology in at risk individuals [41–45].

Here, we used a mouse model that is physiologically relevant to human disease of pregnancy-induced uteroplacental insufficiency to study the effects of IUGR on the molecular and structural events setting the boundaries of the CPd of synaptic plasticity in the dorsal hippocampus, which is functionally and critically linked to memory processes [46]. We focused in the hippocampus for two reasons. First, the hippocampus has a well-defined CPd of synaptic plasticity [24,25,35–38] improving our ability to interpret our data. Second, hippocampal hypoplasia and dysfunction, as seen in our model [16], have been characterized in patients with IUGR [17] and those with schizophrenia [20,21]. Thus, studying the molecular alterations in the events governing the hippocampal CPd will improve our ability to make meaningful contributions about the mechanistic origins of neurodevelopmental disorders and psychopathology in IUGR patients. Because disturbance in the onset, consolidation, or closure of hippocampal CPd of synaptic plasticity leads to impairments, we hypothesized that IUGR would perturb the CPd of synaptic plasticity in the mouse dorsal hippocampus in our model.

MATERIALS AND METHODS

Animals.

Animal procedures were approved by the University of Utah Animal Care Committee (19–02001) and were carried out in accordance with the NIH Guide for the Care and Use of Laboratory Animals. Details about the model are described elsewhere [16,19]. Impregnated C57BL/6J mice (000664, The Jackson Laboratory, Bar Harbor, ME) were confirmed by the presence of vaginal plugs at embryonic day (E) 0.5. At E 12.5, pregnant dams were anesthetized for retroperitoneal implantation of micro-osmotic pump (1007D, 0.5 μl/h, Durect Corporation, Cupertino, CA) containing either 0.5% ethanol (vehicle, sham) or 4000 ng/ul of the thromboxane A_2-analog (TXA), U-46619 dissolved in 0.5% ethanol (Cayman Chemical, Ann Arbor, MI) to deliver 2 μg/h over 7 days. Pups born vaginally at E20–21, were cross-fostered to unmanipulated dams to minimize complications from surgical implantation (Fig 1). Average litter size was 7.5 pups / litter regardless of treatment. We sampled one male pup and one female pup /litter/ age/ treatment group, therefore we used 7 dams/ age (P10, P18, P40)/ treatment group (sham or TXA) = (7 × 3 × 2) = 42 pregnant dams total. All pups from the 42 pregnant dams survived (100% survival rate. In this model, mouse dams receiving U-46619 developed maternal hypertension (mean blood pressures were 20% above sham) 24h after pump implantation, and offspring were 15% growth restricted at birth compared to sham [19]. For our experiments, the mice born after

intrauterine exposure to U-46619 were 18.5% lighter than sham at P18 (14% in males and 22% in females), and deficit resolved by P40 although a trend persisted (p=0.08) as described in the model [19]. Despite weight catchup by P40, hippocampal volumes of the animals used in our experiments were persistently smaller by P40 as reported elsewhere. [16].

Brain harvesting and tissue processing.

Based on available literature [25,35,38–40], we selected 3 times to study specific phases of the CPd in the rodent hippocampus: i) pre-initiation (P10), ii) middle of initiation / consolidation (P18), and iii) ongoing closure (P40). At P10, P18, or P40, mice were anesthetized using ketamine (80–100 μg/g of body weight [BW]) and xylazine (7.5–16 μg/g of BW). Following thoracotomy, transcardiac infusion of normal saline (0.9%) was followed by perfusion with 4% paraformaldehyde (PFA) for fixation. Brains were isolated from the skull, removed, and post-fixed by immersion in 4% PFA overnight (for P10 and P18) or for 2h (for P40) at room temperature (RT), as per modified protocol reported by our group elsewhere [47]. Brains were cryoprotected using a sucrose gradient (5%, 10%, 20%) and once they sank, brains were transferred overnight in 20% sucrose on ice to Johns Hopkins University-School of Medicine Laboratory of Neonatology (RCV laboratory) for further processing, where brains were stored in −80 °C until sectioning. Both sexes were equality represented in all groups and stratification performed, looking for sexual dimorphism.

Western blotting.

Crude brain homogenates from naive mice at P18 were used to validate the antibodies for IHC. Homogenates were cryoprotected using 20% (w/v) glycerol and the Bradford assay was used to determine protein concentrations [48] in a 3:1 (v:v) dilutions of twenty-five μg of protein homogenate and 4X loading buffer (reducing conditions) for western blots. Samples were loaded and run in a 4–20% mini-protean TGX polyacrylamide precast protein gels (Biorad Inc,, Hercules, CA), at 200V, and then transferred to nitrocellulose membrane using TransBlot Turbo Midi-size (Biorad Inc, Hercules, CA). Ponceau S staining was used to verify protein loading and successfully transfer. Membranes were blocked with 2% normal goat serum (NGS) in 0.1% Tween/TBS (TBS-T) instead of the standard bovine albumin (BSA) in order to replicate IHC experimental conditions, as previously reported [47]. Membranes were incubated with primary antibodies at 1:1000 overnight at 4°C. After TBS-T washes, membranes exposed to secondary antibodies for 1h and development using enhanced chemiluminescence (Clarity Western ECL Substrate, Biorad Inc.). To verify that the utility of the primary antibody for IF-IHC we used the following criteria, there must be: i) an identifiable band(s), at molecular weight(s) well described for the target proteins, and ii) absent non-specific binding at molecular weights not reported for the protein, except for well reported post-transcriptional modifications also detected by the antibody.

Standard DAB Immunohistochemistry (IHC) for assessment of astrogliosis.

Brains were cut coronally in 50 μm sections using a freezing microtome. Floating IHC was performed as previously described with rabbit anti-GFAP (DAKO / Agilent Technologies, Santa Clara, CA; 1:1000) followed by goat anti-rabbit antibody (1:200) secondary antibody and DAB as a chromagen. Nissl counterstaining was used for semi-quantitative volumetric

analysis along with GFAP-derived scoring system to assess for astrogliosis [49]. We have reported the hippocampal hypoplasia in this model previously [16]. GFAP scoring was based on the abundance of immunoreactivity (IR) and glial scars evident at low magnification (4X), astrocyte body size, and number and thickness of their branching, as well as presence of astrocytic domain overlapping at higher magnification (20X).

Multi-channel labeled Immunofluorescence (IF)-IHC to assess CPd of synaptic plasticity.

For these experiments coronal brain sections were classified as anterior and containing dorsal hippocampus, when fasciola cinereum appeared next to the dorsal 3rd ventricle and the end of the dorsal subiculum, before the CA3 descended inferiorly to the horizontal level of the fasciculus retroflexus. Following 3 washes with TBS pH 7.2 for 10 min, sections were exposed to sodium citrate buffer pH 6.0 for 90 min at 80°C for antigen retrieval. Permeabilization was achieved by exposure of sections to 0.2% (P10) or 0.4% Triton X in TBS for 15 min at RT. Following blocking step with 10% NGS in 0.1% Tween/TBS for 1h at RT, sections were exposed to various combinations of the following primary antibodies: i) mouse monoclonal IgM anti- PSA-NCAM (Millipore Sigma Inc., Burlington, MA; MAB5324; 1:250); ii) chicken polyclonal IgY anti-PV (Novus Biological LLC, Centennial, CO; NBP2–50036; 1: 250); iii) rabbit polyclonal IgG anti-NPTX2 (ProteinTech Group Inc., Rosemont, IL; 10889–1AP, 1;400); iv) rabbit anti-GAD65/67 (Abcam PLC; Ab11070; 1:400), or v) mouse IgG2b anti myelin basic protein (MBP; Biolegend Inc, San Diego, CA; 808402; 1:2000). Primary antibodies were mixed in 4% NGS in TBS (for PSA-NCAM, and NPTX2) or TBS-T overnight at 4°C. Following overnight incubation, tissues were exposed in the dark for 2h at RT to goat anti-chicken IgY Alexa Fluor 488, goat anti-rabbit or anti mouse conjugated to either Alexa Fluor 568 or 647, emitting red and deep red fluorescence signal, respectively (Thermo Fisher Scientific, Inc, Waltham, MA), mixed in 4% NGS /TBS-T. Lastly, sections were incubated for 5 min in 4’,6-diamidino-2-phenylindole (DAPI) at 1μg/mL in TBS, washed in TBS, and mounted and dried for 30 min prior to coverslip with ProLong Glass Antifade Mountant (Molecular Probes, Life Technologies Corp., Carlsbad, CA). Negative controls included no primary antibody and subtype and species-specific immunoglobulin replacing primary antibody at identical concentrations, as we have previously described [47,50].

Wisteria floribunda lectin (WFA) fluorescent staining for PNN detection.

Fifty μm-thick sections were washed in 1X PBS for 10 min, blocked with 10% NGS in PBS at RT for 90 min, and incubated in green fluorescein conjugated - WFA (Vector Labs, FL-1351–2; at 1:400) in 4% NGS in PBS for 6h at RT. WFA is a lectin that preferentially binds to chondroitin sulfate proteoglycan glycosaminoglycan side chains, which is enriched in PNNs [51,52]. Following PBS washes, slices were incubated in 1 μg/mL DAPI solution for 5 min, washed in PBS, and mounted and dried for 30 min prior to coverslip with ProLong Glass Antifade Mountant (Molecular Probes, Life Technologies Corp.). *WFA-stained PNNs quantification*. PNNs were counted in the dorsal hippocampus embedded in two 50 μm-thick coronal sections, using a Laser Scanning Confocal Microscope LSM700 AxioObserver from Carl Zeiss AG (Oberkochen, Germany). Area of each subfield was measured in triplicate using the free-drawing function of ImageJ/Fiji software. Following transformation to mm^2 the average area of each subfield was used to adjust PNN counts.

Confocal microscopy.

Z-stacks were taken at 1440 × 1440 pixels, 16-bit depth, and averaged X2, captured using a Plan-Apochromat 63X/1.4 Oil DIC M27 objective and 1.0 zoom to produce an uncompressed image of 101.54 × 101.54 μm at the most dorsal CA1 (two fields) and the most temporal CA3 (four fields), as represent in **panel B of** figure 1. Z-stacks were set for slicing at 1 air unit (0.8 μm) to the maximal wavelength used in the experiments (639 nm) using a Laser Scanning Confocal Microscope LSM700 AxioObserver from Carl Zeiss AG (Oberkochen, Germany). Only exception was for MBP staining where field were taken at 0.5 zoom, which captures and are of 203.08 × 203.08 μm per panel, taken at 0.5 air unit (0.3 μm), to better reconstruct myelinated filaments as described ahead. In all cases, same IF-IHC protocol specifications were followed in all repeats of each experiments, as well as same configurations for pinhole, gain and offset were reused to capture repeats for each experiment for the same combinations. Detection wavelengths were: 300–483 nm for DAPI, 493 to 550 nm for Alexa 488, 560–600 nm for Alexa 568, 644–800 nm for Alexa 647. Z-stacks were saved in .czi format for processing uncompressed.

Image processing using Imaris.

Image processing was performed using Imaris x64 v9.8 software (Bitplane AG. Belfast, UK). In all cases, we collected 3 main measurements per IF channel source: i) counts (i.e. cells, puncta), ii) per count and total (sum) volume (in μm^3), and iii) total intensity of immunoreactivity (IF, in arbitrary units [A.U]). All of these measurements were reported adjusted for the volume (μm^3) of region of interest within the z-stack in which they were measured. Each provide different information related to abundance of the objects (counts, total volume, and total IF), and the size of the objects (volume per count). Additionally, only specific to PV^+ INs, surface area (μm^2) was also calculated to derive the number of NPTX2 $^+$ synaptic boutons (puncta) in contact with their membrane. These measurements were obtained as described ahead. *Volumetric reconstruction:* following automatic creation of an algorithm and definition of channel source and level of surface detailing, the detected surface renderings were adjusted automatically after background subtraction and masking to zero voxels inside surface. Split touching object function is used with the seed point diameter set to the average diameter of the cell/object of interest. *Dendritic complexity reconstruction:* an automatic dendrite detection protocol was used using the green channel (fluorescein conjugated for WFA [cells = 22 – 47/treatment/ CA subfield] or Alexa 488 conjugated for PV^+ IN Sholl analysis [cells = 28 – 37/treatment/ CA subfield]). We created new filaments starting with the automatic algorithm setting to calculate diameter of filament. Starting points, the largest dendritic diameter, and seed points, the smallest dendritic diameter, were identified in slice mode and adjusted using automatic and manual thresholds. Settings included the removal of seed points around set diameter of the starting point sphere region to avoid excess or false filament creation around towards area of intense IF (i.e. soma). Detected points were then automatically connected with lines following the image intensity. Similar filament algorithm was used for the measurement of the length of MBP^+ myelinated axons.

Statistics.

Shapiro-Wills test confirmed non-normal distribution of the data. Thus, non-parametric Mann Whitney U test was applied at each separate time point and stratified by sex when appropriate. All results are presented as box and whisker plots, where each box was limited by the 25th and 75th percentiles and the solid line represented the median with all experimental data points are shown. Outliers beyond 1.5 × interquartile range (IQR) from median and extremes beyond 3 × IQR from median are represented. Non-parametric Spearman Rho correlations were used, and a best-fit regression line was calculated to determine relationship between i) GAD 65/67 puncta per neuron with PSA-NCAM abundance at P18, and ii) NPTX2 abundance (total volume and total and per PV$^+$ surface area [μm^2] puncta counts) with MBP$^+$ axonal length or PNN characteristics. These relationships were presented as scatter plot with fitted line and 95% confidence interval boundaries. Significance was assigned by p-value ≤ 0.05 in all cases. Analysis was performed using IBM SPSS Statistics 24v (IBM Corporation, Armonk, NY).

RESULTS

Minimal astrogliosis in dorsal hippocampus of IUGR mice at P18.

Despite the hippocampal hypoplasia reported in this IUGR model at P40 [16], no differences were identified in astrogliosis in the dorsal hippocampus at P18 in either sex using a well described GFAP immunoreactivity (IR) scoring [47,49,50,53,54]. Both sham and IUGR mice had median GFAP scores of 3 IQR (3–5) regardless of sex. Representative microphotographs are shown in Supplemental Fig 1. Correlations between hippocampal hypoplasia and GFAP IR were not significant (**data not shown**).

Increased abundance of GAD 65/67 $^+$ synaptic boutons in IUGR mice at P18.

GABAergic development, particularly from PV$^+$ INs, is a mandatory trigger for the initiation of the CPd of postnatal synaptic plasticity. No difference was observed in the number or volume of either PV$^+$ INs or GAD 65/67$^+$ puncta at P10 between groups (Fig 2A–D), although some variability was observed in the abundance of GAD 65/67$^+$ puncta as suggested in example panels **2A$_2$** vs. **2B$_2$**. This apparent difference did not reach significance (p=0.18, n=8 per group, **data not shown**). At P18, no difference in PV$^+$ INs was identified (Fig 2E); however, GAD 65/67$^+$ puncta were more abundant in IUGR mice compared to shams in CA1 (p=0.001) and CA3 (p=0.03) pyramidal cell layer (Py, Supplemental Figure 2A). As a result, GAD 65/67 total volume in CA1 of IUGR mice was 42.8% higher than in shams (p= 0.008, Fig 2F$_1$) at P18. Likewise, at P18, the total GAD 65/67 $^+$ volume (sum of the volume of all puncta) and the mean volume of the GAD 65/67$^+$ puncta were 44% (p=0.04, Fig 2F$_1$) and 31.4% (p=0.02, Fig 2F$_2$) higher in the CA3 of IUGR mice compared to sham. When calculated by pyramidal cell (using DAPI stained nuclei as surrogate, as the most abundant cell subtype within the Py layer), IUGR mice had 30.2% (p= 0.001) and 23.5% (p= 0.03) more GAD65/67$^+$ puncta per neuron in the CA1 and CA3 pyramidal cell layers (Py), respectively (Fig 2F$_3$ & Fig 2G$_1$–G$_2$). At P40, the abundance of GAD 65/67$^+$ synaptic boutons was similar between treatment groups (Fig 2H$_1$–H$_2$), as a result of a 59% (p=0.004) and 49% (p=0.01) increase in the number of

GAD 65/67 $^{+}$ puncta in the CA1 and CA3 of sham animals, respectively, from P18 to P40 (Supplemental fig 2B & 2C).

PSA-NCAM is less abundant in IUGR mice at P18.

The polysialylated modification of NCAM (PSA-NCAM) located in the membrane of pyramidal cells of the developing hippocampus limit the formation of perisomatic inhibitory GABAergic synapses, predominantly from PV^{+} INs needed to initiate the CPd [40]. Expression of PSA-NCAM, which was abundant in neuronal progenitor cells of the DG (internal control, **not shown**), was modest in the CA at P18. Thus, we tested if PSA-NCAM expression decreased to permit the accelerated GABAergic synaptic formation in IUGR mice at P18. Indeed, CA3 PSA-NCAM total volume and IF were decreased by 75% (p=0.01) and 73.2% (p=0.01) respectively in the oriens layer (Or) of IUGR mice compared to. shams (Fig $3A_1$ & $3A_2$). Similar trends were documented in the radiatum layer (Rd) (Fig $3B_1$ & $3B_2$). Because most PV $^{+}$ INs synaptic boutons target perisomatic domains of the pyramidal cell, thus abundance in the Py would better relate to the changes documented in GAD65/67. PSA-NCAM total volume and IR was decreased by 34.6% (p=0.01, Fig $3C_1$) and 36.2% (p=0.03, Fig $3C_2$) respectively in the CA1 Py of IUGR mice at P18. Similarly, PSA-NCAM total volume trended to be lower in the CA3 (p=0.10), while PSA-NCAM IF was decreased by 38.5% (p=0.01, Fig $3C_2$) at P18. In addition, because PSA- NCAM decrease permits inhibitory synapse formation, we tested the associations between GAD 65/67 and PSA-NCAM in the model at P18. Both, GAD 65/67^{+} puncta count (r = − 043, p=0.02), and total volume (r = −0.63, p=0.001) inversely correlated with PSA-NCAM IF at P18. Similarly, GAD 65/67 number of puncta per neuron (r = −0.55, p=0.005; Fig $3E_1$) and volume per neuron (r= −0.62, p=0.001; Fig $3E_2$) inversely correlated to PSA-NCAM abundance in the CA1 Py. Similar trends were observed in the CA3 Py (**data not shown**). Representative z-stack renderings of multichannel-IF immunostaining experiments are shown (Fig. $3D_1$ & $3D_2$).

Decreased NPTX2 $^{+}$ excitatory puncta in the dorsal CA3 of IUGR mice at P18 and P40.

Following the development of inhibitory inputs into pyramidal cells, NPTX2 is upregulated leading to accelerated formation of excitatory synapses. Thus, we tested if accelerated GABAergic development in IUGR mice would result in increased NPTX2. However, we found the opposite result. The number of NPTX2 $^{+}$ puncta was decreased by 64.3% in the CA3 Rd (p<0.001, Fig $4A_1$), and by 32.1% in the CA3 Py (p=0.004, Fig $4B_1$) in IUGR mice. Accordingly, NPTX2 total volume and IF were also decreased by 72.2% (p=0.001, Fig $4A_2$) and 61.3% (p=0.02, Fig $4A_3$) in CA3 Rd, and by 36.8% (p<0.001, Fig $4B_2$) and 42.4% (p=0.02, Fig $4B_3$) in the CA3 Py, respectively in IUGR mice. Similar trends were documented in the CA1 Rd and Py. Representative z-stack renderings of are shown (Fig. $4C_1$ to $4C_4$). At P40, the deficits in NPTX2 were persistent, but attenuated (Fig 5). Thus, NPTX2 total volumes were decreased by 31.9% in the CA3 Rd (p=0.05, Fig $5A_2$) and by 41.3% in the CA3 Py (p=0.01, Fig $5B_2$) in IUGR mice vs. sham. However, deficits in NPTX2 levels documented in IUGR mice coexisted with minimal alteration in the dendritic complexity of PV $^{+}$ INs via Sholl analysis (Fig 5C). Representative renderings of NPTX2 $^{+}$ puncta (red channel) and PV $^{+}$ IN dendritic structure (green channel) are shown (Fig 5D).

Disrupted myelination in the CA3 of IUGR mice is sexually dimorphic.

Oligodendrocyte maturation and myelination is one of the events marking the closure of the CPd of synaptic plasticity [31]. IUGR mice had decreased length of myelinated (MBP^+) axons in the CA3 (p= 0.008 vs. sham; Fig $6A_1$), along with decreased myelin surface area (p= 0.01 vs. sham; Fig $6A_2$) and myelinated axonal volume (p= 0.04 vs. sham; Fig $6A_3$) at P40. MBP^+ axons adjusted by the number of neurons (DAPI stained) further supports impaired myelination and no decreased number of neurons (p= 0.002 vs. sham; Fig $6A_4$). All the events reported until now, including $NPTX2^+$ puncta analysis, have not shown sexual dimorphism. However, sex stratification demonstrated that disrupted myelination only occurred in female IUGR mice (Fig $6A_1$ to $6A_4$). All, length (r=0.44, p=0.05), surface area (r= 0.45, p=0.04), and volume (r= 0.46, p=0.04) of myelinated axons directly correlated with the abundance of $NPTX2^+$ puncta in the CA3 (Supplemental Fig 3). The strength of these associations was stronger in the Rd, layer within the CA3 with the strongest NPTX2 expression, as showed previously. Rendering of representative z-stacks and their respective filament reconstructions using Imaris software are shown for CA1 (Fig $6B_1$) and CA3 (Fig $6B_2$) from female mice. MBP^+ axonal length directly correlated with NPTX2 volume in the Rd (r= 0.63, p=0.006, Fig 6C)

Disruption in volume, and density of PNNs in the CA1 and CA3 of IUGR mice at P40.

PNNs provide the support needed to stabilize $NPTX2^+$ excitatory synapses on PV^+ INs, which lead to the closure of the CPd of synaptic plasticity. We found no difference in the number of PNNs in the dorsal hippocampus between IUGR mice and shams at P40 (Fig $7A_1$). Counts per hippocampal subfield (CA1 and CA3) did not showed differences either (**data not shown**), although in the CA3 PNN counts trended to be lower in IUGR mice of both sexes (Fig $7A_1$). However, the volumes of PNNs (in μm^3) within the CA1 and CA3 were decreased by 30.7% (p = 0.03) and 43.7% (p=0.004), respectively at P40 (Fig $7A_2$). Similarly, the density (IF) of those PNNs was also decreased in the CA1 (p= 0.008) and CA3 (p<0.001) (Fig $7A_3$). Sex stratification demonstrated that the decrease in volume (Fig $7A_2$') and density (Fig $7A_3$') of PNNs occurred exclusively in the female CA1 and CA3. Representative rendering of surface reconstructions for PNNs located in the female CA1 (Fig $7B_{1–2}$) and CA3 (Fig $7B_{3–4}$) are shown. Next, we studied the relationships between the PNN disruption with $NPTX2^+$ puncta in the Py. Density of PNN, measured as IF, directly correlated with the number of $NPTX2^+$ puncta per 1000 μm^3 of volume (Fig $7C_1$) and per 100 μm^2 of PV^+ IN surface area (SA, Fig $7C_2$) in the CA1 and CA3 Py. The strength of relationships between $NPTX2^+$ puncta and PNN disruption, irrespective of treatment group, was assessed using Spearman Rho correlation stratified by sex as shown in heatmap (Fig 8). Although, no difference in directionality of the relationships was observed between males and female in the CA3, sexual dimorphism was observed in the CA1 subfield analysis. The correlation between the abundance of $NPTX2^+$ puncta per 100 μm^2 of PV^+ IN SA with PNN volumes was direct in female mice, while it was inverse in male mice.

DISCUSSION

Here, we delineated for the first time the effects of hypertensive disease of pregnancy-induced IUGR on the molecular and structural initiation, consolidation, and closure of the

postnatal CPd of synaptic plasticity in the mouse dorsal hippocampus. Earlier than expected developmental GABAergic maturation and PSA-NCAM decline suggest premature onset of the CPd. However, NPTX2 decrease expression in the dorsal CA Rd and Py, and localization in excitatory synapses into PV^+ INs argue against appropriate consolidation of the CPd in the hippocampus. Lastly, perturbed axonal myelination (MBP^+), which correlates with NPTX2 deficit, along with decreased volume and integrity of the PNNs in the dorsal CA of IUGR mice in early adulthood, supports impaired closure of the postnatal CPd. Together, our findings show that a perturbed developmental pattern of events governing the postnatal CPd in the dorsal hippocampus would likely affect the intricate balance between excitatory and inhibitory neuronal development, which may underlie the learning and memory deficits observed in our adult IUGR mice [16] and the cognitive disorders seen in human IUGR offspring [12,13].

The postnatal CPd of synaptic plasticity has been extensively studied in the visual cortex [31,55–58], and more recently in the hippocampus, where sequential waves for learning enable the acquisition of complex functions as elegantly described by Albertini et al [35]. The complex events limiting the boundaries of these critical periods emerge from the quality and strength of interactions between excitatory pyramidal cells and PV^+ INs, particularly the later which is paramount in the establishment of the excitatory : inhibitory balance [59]. Thus, our experiments were centered on the development of the GABAergic circuit and the temporal shift in events governing the postnatal CPd of synaptic plasticity in the hippocampus after IUGR.

In our hypertensive disease of pregnancy -induced model and other IUGR models, hippocampal hypoplasia and memory deficits have been described [16] resembling those seen in human IUGR offspring [4,5,11,14,60]. Alterations in several of the events framing the postnatal CPd of synaptic development in the hippocampus may explain some of our previous findings [16]. Here, we described that although the number of PV^+ INs remains unchanged, the number, total volume, and IF intensity of GAD $65/67^+$ synaptic boutons are prematurely increased by P18, a time at which they inversely correlated with the decrease in PSA-NCAM abundance in IUGR offspring. The GABAergic maturation that follows is pivotal for initiation of the CPd, and thus genetic silencing of GAD prevents the initiation of this period [59,61]. The maturation, connectivity, and activity of PV^+ INs are also controlled by the extracellular matrix molecules, such as PSA-NCAM and later the formation of PNNs [62,63]. The decrease in PSA modification of NCAM, which prevents cell adhesion, connectivity, and GABAergic development [64,65], facilitate formation of perisomatic GABAergic synaptic boutons and consolidation of inhibitory networks [66,67] Thus, the accelerated PSA-NCAM decline, and GAD $65/67^+$ synaptic boutons development in the dorsal CA1 and CA3 of IUGR offspring suggest premature PV^+ IN maturation and initiation of the postnatal CPd of synaptic plasticity.

NPTX2, an immediate early gene (IEG), is produced by CA pyramidal cells to mediate activity-dependent plasticity [68] pivotal for memory formation [69,70]. NPTX2 is known to accumulate in excitatory synapses into PV^+ INs [28] to consolidate the postnatal CPd of synaptic plasticity by enhancing PV^+ IN function, essential for excitatory :inhibitory balance and memory formation [32,71–74]. In our model of IUGR, we identify decreased

NPTX2 in pyramidal cells at P18, which in a lesser degree persists by P40. Thus, even when PV^+ INs numbers are preserved and their perisomatic synaptic boutons to pyramidal cells are increased in IUGR offspring, this does not result in NPTX2 upregulation. To the contrary, we speculate that accelerated and increased GABAergic maturation may negatively impact CA1 and CA3 pyramidal cell activity, resulting in NPTX2 downregulation. Knowing that NPTX2 is also necessary to enhance and maintain PNN formation in primary cortical neurons [75], the decrease in volume and intensity of the PNNs stained with WFA, may also be a downstream effect, as suggested by the direct correlation between NPTX2 and WFA staining at P40. Although we document sexual dimorphism in the relationship between NPTX2 and PNN formation in the CA1, with higher $NPTX2^+$ puncta in PV^+ INs inversely correlated with PNN volumes; neither NPTX2 abundance, nor PNN volumes are disrupted in the CA1 of IUGR male mice. Thus, these relationships are important to dissect, but do not play a major role in the characterization of the perturbance of the CPd in our model. Perturbations in the events setting the consolidation and closure of the CPd in the dorsal hippocampus, are also suggested by the impaired myelination reported here. Effect in oligodendroglia and myelination has been reported previously in the IUGR model used for our experiments [15], and a sheep model [76], along with multiple other models [77–79]. Myelination along with the formation of PNNs in PV^+ INs close the CPd of synaptic plasticity [31]. Thus, our results in the context of previous evidence support the thesis that IUGR delays the closure of the postnatal CPd of synaptic plasticity in the dorsal hippocampus.

We acknowledge several limitations in this study. First, the data presented here are only describing the changes seen in the dorsal hippocampus of IUGR offspring in our model, but mechanistic aspects of how these events occur and the downstream outcomes are still under investigation. Study of miniature inhibitory postsynaptic currents measured in pyramidal cells using patch clamping followed by GABAergic blockade manipulation is among the next steps to fully interpret the effect of the increase in GABAergic synaptic boutons and the link with decrease NPTX2 expression and PNN formation. Study of many other events governing the CPd is needed, for example evaluating the upstream cascades, such as changes in BDNF are warranted, as in the visual cortex BDNF overexpression is sufficient to close the critical period of synaptic plasticity [80]. Lastly, we have focused on the study of the events governing the postnatal CPd within the hippocampal CA, understanding that future studies must incorporate the evaluation of the dentate gyrus, entorhinal cortex, and amygdala to better interpret the functional integration of the limbic system resulting from IUGR.

Conclusions.

To our knowledge, this is the first study evaluating the postnatal CPd of synaptic plasticity in the dorsal hippocampus of IUGR offspring. Our results support a premature opening of this period led by early GABAergic development and decline in PSA modification of NCAM, but also a delayed consolidation and closure supported by decreased NPTX2 accumulation impairing excitatory synapses formation into PV^+ INs and concomitantly disturbing PNN formation and myelination. Altogether, our data support the current thesis that premature onset plus abnormal lengthening of the CPd of synaptic plasticity in the dorsal hippocampus is likely linked to neurodevelopmental and neuropsychiatric disorders [41]. It remains to be

determined what the mechanisms are driving such perturbed timing in IUGR and whether such perturbation is amendable to therapy in postnatal life.

Supplementary Material

Refer to Web version on PubMed Central for supplementary material.

ACKNOWLEDGEMENTS

The authors thank Mrs. Deborah Flock for her technical support and Mrs. Rosie Silva for her administrative assistance.

FUNDING SOURCES

National Institutes of Health (KO8NS096115 – RC-V and RO1NS086945 – CF), the JHU-SOM Clinician Scientist Award (RC-V), The Thomas Wilson Foundation (RC-V).

DATA AVAILABILITY STATEMENT.

All data generated or analyzed during this study are included in this article and its supplementary material files. Further enquiries can be directed to the corresponding author

REFERENCES

1. Lee AC, Katz J, Blencowe H, Cousens S, Kozuki N, Vogel JP, Adair L, Baqui AH, Bhutta ZA, Caulfield LE, Christian P, Clarke SE, Ezzati M, Fawzi W, Gonzalez R, Huybregts L, Kariuki S, Kolsteren P, Lusingu J, Marchant T, Merialdi M, Mongkolchati A, Mullany LC, Ndirangu J, Newell ML, Nien JK, Osrin D, Roberfroid D, Rosen HE, Sania A, Silveira MF, Tielsch J, Vaidya A, Willey BA, Lawn JE, Black RE, Group CS-PBW: National and regional estimates of term and preterm babies born small for gestational age in 138 low-income and middle-income countries in 2010. Lancet Glob Health 2013;1:e26–36. [PubMed: 25103583]
2. Figueras F, Gardosi J: Intrauterine growth restriction: new concepts in antenatal surveillance, diagnosis, and management. Am J Obstet Gynecol 2011;204:288–300. [PubMed: 21215383]
3. Mandruzzato G, Antsaklis A, Botet F, Chervenak FA, Figueras F, Grunebaum A, Puerto B, Skupski D, Stanojevic M, Wapm: Intrauterine restriction (IUGR). J Perinat Med 2008;36:277–281. [PubMed: 18598115]
4. McIntire DD, Bloom SL, Casey BM, Leveno KJ: Birth weight in relation to morbidity and mortality among newborn infants. N Engl J Med 1999;340:1234–1238. [PubMed: 10210706]
5. Gardosi J, Madurasinghe V, Williams M, Malik A, Francis A: Maternal and fetal risk factors for stillbirth: population based study. BMJ 2013;346:f108. [PubMed: 23349424]
6. Egana-Ugrinovic G, Sanz-Cortes M, Figueras F, Couve-Perez C, Gratacos E: Fetal MRI insular cortical morphometry and its association with neurobehavior in late-onset small-for-gestational-age fetuses. Ultrasound Obstet Gynecol 2014;44:322–329. [PubMed: 24616027]
7. Sanz-Cortes M, Egana-Ugrinovic G, Zupan R, Figueras F, Gratacos E: Brainstem and cerebellar differences and their association with neurobehavior in term small-for-gestational-age fetuses assessed by fetal MRI. Am J Obstet Gynecol 2014;210:452 e451–458. [PubMed: 24315862]
8. Egana-Ugrinovic G, Sanz-Cortes M, Figueras F, Bargallo N, Gratacos E: Differences in cortical development assessed by fetal MRI in late-onset intrauterine growth restriction. Am J Obstet Gynecol 2013;209:126 e121–128. [PubMed: 23583839]
9. Egana-Ugrinovic G, Savchev S, Bazan-Arcos C, Puerto B, Gratacos E, Sanz-Cortes M: Neurosonographic assessment of the corpus callosum as imaging biomarker of abnormal neurodevelopment in late-onset fetal growth restriction. Fetal Diagn Ther 2015;37:281–288. [PubMed: 25659952]

10. Figueras F, Eixarch E, Meler E, Iraola A, Figueras J, Puerto B, Gratacos E: Small-for-gestational-age fetuses with normal umbilical artery Doppler have suboptimal perinatal and neurodevelopmental outcome. Eur J Obstet Gynecol Reprod Biol 2008;136:34–38. [PubMed: 17434250]
11. Baschat AA: Neurodevelopment after fetal growth restriction. Fetal Diagn Ther 2014;36:136–142. [PubMed: 23886893]
12. Tolsa CB, Zimine S, Warfield SK, Freschi M, Sancho Rossignol A, Lazeyras F, Hanquinet S, Pfizenmaier M, Huppi PS: Early alteration of structural and functional brain development in premature infants born with intrauterine growth restriction. Pediatr Res 2004;56:132–138. [PubMed: 15128927]
13. Lodygensky GA, Seghier ML, Warfield SK, Tolsa CB, Sizonenko S, Lazeyras F, Huppi PS: Intrauterine growth restriction affects the preterm infant's hippocampus. Pediatr Res 2008;63:438–443. [PubMed: 18356754]
14. Gilchrist C, Cumberland A, Walker D, Tolcos M: Intrauterine growth restriction and development of the hippocampus: implications for learning and memory in children and adolescents. Lancet Child Adolesc Health 2018;2:755–764. [PubMed: 30236384]
15. Chang JL, Bashir M, Santiago C, Farrow K, Fung C, Brown AS, Dettman RW, Dizon MLV: Intrauterine Growth Restriction and Hyperoxia as a Cause of White Matter Injury. Dev Neurosci 2018;40:344–357. [PubMed: 30428455]
16. Brown AS, Wieben M, Murdock S, Chang J, Dizon MLV, St Pierre M, Chavez-Valdez R, Dorsky RI, Fung CM: Intrauterine Growth Restriction Causes Abnormal Embryonic Dentate Gyrus Neurogenesis in Mouse Offspring That Leads to Adult Learning and Memory Deficits. eNeuro 2021;8
17. Mallard EC, Rehn A, Rees S, Tolcos M, Copolov D: Ventriculomegaly and reduced hippocampal volume following intrauterine growth-restriction: implications for the aetiology of schizophrenia. Schizophr Res 1999;40:11–21. [PubMed: 10541002]
18. Fung CM, Yang Y, Fu Q, Brown AS, Yu B, Callaway CW, Li J, Lane RH, McKnight RA: IUGR prevents IGF-1 upregulation in juvenile male mice by perturbing postnatal IGF-1 chromatin remodeling. Pediatr Res 2015;78:14–23. [PubMed: 25826117]
19. Fung C, Brown A, Cox J, Callaway C, McKnight R, Lane R: Novel thromboxane A2 analog-induced IUGR mouse model. J Dev Orig Health Dis 2011;2:291–301. [PubMed: 25141265]
20. Ray KL, Lesh TA, Howell AM, Salo TP, Ragland JD, MacDonald AW, Gold JM, Silverstein SM, Barch DM, Carter CS: Functional network changes and cognitive control in schizophrenia. Neuroimage Clin 2017;15:161–170. [PubMed: 28529872]
21. Ragland JD, Layher E, Hannula DE, Niendam TA, Lesh TA, Solomon M, Carter CS, Ranganath C: Impact of schizophrenia on anterior and posterior hippocampus during memory for complex scenes. Neuroimage Clin 2017;13:82–88. [PubMed: 27942450]
22. Hensch TK: Critical period plasticity in local cortical circuits. Nat Rev Neurosci 2005;6:877–888. [PubMed: 16261181]
23. Bessieres B, Jia M, Travaglia A, Alberini CM: Developmental changes in plasticity, synaptic, glia, and connectivity protein levels in rat basolateral amygdala. Learn Mem 2019;26:436–448. [PubMed: 31615855]
24. Travaglia A, Bisaz R, Cruz E, Alberini CM: Developmental changes in plasticity, synaptic, glia and connectivity protein levels in rat dorsal hippocampus. Neurobiol Learn Mem 2016;135:125–138. [PubMed: 27523749]
25. Travaglia A, Bisaz R, Sweet ES, Blitzer RD, Alberini CM: Infantile amnesia reflects a developmental critical period for hippocampal learning. Nat Neurosci 2016;19:1225–1233. [PubMed: 27428652]
26. Lisman J, Schulman H, Cline H: The molecular basis of CaMKII function in synaptic and behavioural memory. Nat Rev Neurosci 2002;3:175–190. [PubMed: 11994750]
27. Lisman J, Yasuda R, Raghavachari S: Mechanisms of CaMKII action in long-term potentiation. Nat Rev Neurosci 2012;13:169–182. [PubMed: 22334212]

28. Chang MC, Park JM, Pelkey KA, Grabenstatter HL, Xu D, Linden DJ, Sutula TP, McBain CJ, Worley PF: Narp regulates homeostatic scaling of excitatory synapses on parvalbumin-expressing interneurons. Nat Neurosci 2010;13:1090–1097. [PubMed: 20729843]
29. Angulo MC, Lambolez B, Audinat E, Hestrin S, Rossier J: Subunit composition, kinetic, and permeation properties of AMPA receptors in single neocortical nonpyramidal cells. J Neurosci 1997;17:6685–6696. [PubMed: 9254681]
30. Fournier AE, GrandPre T, Strittmatter SM: Identification of a receptor mediating Nogo-66 inhibition of axonal regeneration. Nature 2001;409:341–346. [PubMed: 11201742]
31. Lee HHC, Bernard C, Ye Z, Acampora D, Simeone A, Prochiantz A, Di Nardo AA, Hensch TK: Genetic Otx2 mis-localization delays critical period plasticity across brain regions. Mol Psychiatry 2017;22:680–688. [PubMed: 28194008]
32. Xiao MF, Xu D, Craig MT, Pelkey KA, Chien CC, Shi Y, Zhang J, Resnick S, Pletnikova O, Salmon D, Brewer J, Edland S, Wegiel J, Tycko B, Savonenko A, Reeves RH, Troncoso JC, McBain CJ, Galasko D, Worley PF: NPTX2 and cognitive dysfunction in Alzheimer's Disease. Elife 2017;6
33. Makinodan M, Rosen KM, Ito S, Corfas G: A critical period for social experience-dependent oligodendrocyte maturation and myelination. Science 2012;337:1357–1360. [PubMed: 22984073]
34. Akbik F, Cafferty WB, Strittmatter SM: Myelin associated inhibitors: a link between injury-induced and experience-dependent plasticity. Exp Neurol 2012;235:43–52. [PubMed: 21699896]
35. Alberini CM, Travaglia A: Infantile Amnesia: A Critical Period of Learning to Learn and Remember. J Neurosci 2017;37:5783–5795. [PubMed: 28615475]
36. Zhang Y, Smolen P, Alberini CM, Baxter DA, Byrne JH: Computational model of a positive BDNF feedback loop in hippocampal neurons following inhibitory avoidance training. Learn Mem 2016;23:714–722. [PubMed: 27918277]
37. Ye X, Kapeller-Libermann D, Travaglia A, Inda MC, Alberini CM: Direct dorsal hippocampal-prelimbic cortex connections strengthen fear memories. Nat Neurosci 2017;20:52–61. [PubMed: 27869801]
38. Carstens KE, Phillips ML, Pozzo-Miller L, Weinberg RJ, Dudek SM: Perineuronal Nets Suppress Plasticity of Excitatory Synapses on CA2 Pyramidal Neurons. J Neurosci 2016;36:6312–6320. [PubMed: 27277807]
39. Gao X, Castro-Gomez S, Grendel J, Graf S, Susens U, Binkle L, Mensching D, Isbrandt D, Kuhl D, Ohana O: Arc/Arg3.1 mediates a critical period for spatial learning and hippocampal networks. Proc Natl Acad Sci U S A 2018;115:12531–12536. [PubMed: 30442670]
40. Guirado R, Perez-Rando M, Sanchez-Matarredona D, Castren E, Nacher J: Chronic fluoxetine treatment alters the structure, connectivity and plasticity of cortical interneurons. Int J Neuropsychopharmacol 2014;17:1635–1646. [PubMed: 24786752]
41. Meredith RM: Sensitive and critical periods during neurotypical and aberrant neurodevelopment: a framework for neurodevelopmental disorders. Neurosci Biobehav Rev 2015;50:180–188. [PubMed: 25496903]
42. Aceti M, Creson TK, Vaissiere T, Rojas C, Huang WC, Wang YX, Petralia RS, Page DT, Miller CA, Rumbaugh G: Syngap1 haploinsufficiency damages a postnatal critical period of pyramidal cell structural maturation linked to cortical circuit assembly. Biol Psychiatry 2015;77:805–815. [PubMed: 25444158]
43. Xing B, Li YC, Gao WJ: GSK3beta Hyperactivity during an Early Critical Period Impairs Prefrontal Synaptic Plasticity and Induces Lasting Deficits in Spine Morphology and Working Memory. Neuropsychopharmacology 2016;41:3003–3015. [PubMed: 27353310]
44. Iafrati J, Orejarena MJ, Lassalle O, Bouamrane L, Gonzalez-Campo C, Chavis P: Reelin, an extracellular matrix protein linked to early onset psychiatric diseases, drives postnatal development of the prefrontal cortex via GluN2B-NMDARs and the mTOR pathway. Mol Psychiatry 2014;19:417–426. [PubMed: 23752244]
45. Bitanihirwe BK, Mauney SA, Woo TU: Weaving a Net of Neurobiological Mechanisms in Schizophrenia and Unraveling the Underlying Pathophysiology. Biol Psychiatry 2016;80:589–598. [PubMed: 27113498]

46. Fanselow MS, Dong HW: Are the dorsal and ventral hippocampus functionally distinct structures? Neuron 2010;65:7–19. [PubMed: 20152109]
47. Chavez-Valdez R, Lechner C, Emerson P, Northington FJ, Martin LJ: Accumulation of PSA-NCAM marks nascent neurodegeneration in the dorsal hippocampus after neonatal hypoxic-ischemic brain injury in mice. J Cereb Blood Flow Metab 2021;41:1039–1057. [PubMed: 32703109]
48. Bradford MM: A rapid and sensitive method for the quantitation of microgram quantities of protein utilizing the principle of protein-dye binding. Anal Biochem 1976;72:248–254. [PubMed: 942051]
49. Chavez-Valdez R, Emerson P, Goffigan-Holmes J, Kirkwood A, Martin LJ, Northington FJ: Delayed injury of hippocampal interneurons after neonatal hypoxia-ischemia and therapeutic hypothermia in a murine model. Hippocampus 2018;28:617–630. [PubMed: 29781223]
50. Lechner CR, McNally MA, St Pierre M, Felling RJ, Northington FJ, Stafstrom CE, Chavez-Valdez R: Sex specific correlation between GABAergic disruption in the dorsal hippocampus and flurothyl seizure susceptibility after neonatal hypoxic-ischemic brain injury. Neurobiol Dis 2021;148:105222. [PubMed: 33309937]
51. Reinhard SM, Rais M, Afroz S, Hanania Y, Pendi K, Espinoza K, Rosenthal R, Binder DK, Ethell IM, Razak KA: Reduced perineuronal net expression in Fmr1 KO mice auditory cortex and amygdala is linked to impaired fear-associated memory. Neurobiol Learn Mem 2019;164:107042. [PubMed: 31326533]
52. Pizzorusso T, Medini P, Berardi N, Chierzi S, Fawcett JW, Maffei L: Reactivation of ocular dominance plasticity in the adult visual cortex. Science 2002;298:1248–1251. [PubMed: 12424383]
53. Goffigan-Holmes J, Sanabria D, Diaz J, Flock D, Chavez-Valdez R: Calbindin-1 Expression in the Hippocampus following Neonatal Hypoxia-Ischemia and Therapeutic Hypothermia and Deficits in Spatial Memory. Dev Neurosci 2019:1–15.
54. McNally MA, Chavez-Valdez R, Felling RJ, Flock DL, Northington FJ, Stafstrom CE: Seizure Susceptibility Correlates with Brain Injury in Male Mice Treated with Hypothermia after Neonatal Hypoxia-Ischemia. Dev Neurosci 2019:1–10.
55. Fagiolini M, Fritschy JM, Low K, Mohler H, Rudolph U, Hensch TK: Specific GABAA circuits for visual cortical plasticity. Science 2004;303:1681–1683. [PubMed: 15017002]
56. Gu Y, Huang S, Chang MC, Worley P, Kirkwood A, Quinlan EM: Obligatory role for the immediate early gene NARP in critical period plasticity. Neuron 2013;79:335–346. [PubMed: 23889936]
57. Jiang B, Huang S, de Pasquale R, Millman D, Song L, Lee HK, Tsumoto T, Kirkwood A: The maturation of GABAergic transmission in visual cortex requires endocannabinoid-mediated LTD of inhibitory inputs during a critical period. Neuron 2010;66:248–259. [PubMed: 20435001]
58. Huang ZJ, Kirkwood A, Pizzorusso T, Porciatti V, Morales B, Bear MF, Maffei L, Tonegawa S: BDNF regulates the maturation of inhibition and the critical period of plasticity in mouse visual cortex. Cell 1999;98:739–755. [PubMed: 10499792]
59. Reh RK, Dias BG, Nelson CA 3rd, Kaufer D, Werker JF, Kolb B, Levine JD, Hensch TK: Critical period regulation across multiple timescales. Proc Natl Acad Sci U S A 2020;117:23242–23251. [PubMed: 32503914]
60. Miller SL, Huppi PS, Mallard C: The consequences of fetal growth restriction on brain structure and neurodevelopmental outcome. J Physiol 2016;594:807–823. [PubMed: 26607046]
61. Hensch TK, Fagiolini M, Mataga N, Stryker MP, Baekkeskov S, Kash SF: Local GABA circuit control of experience-dependent plasticity in developing visual cortex. Science 1998;282:1504–1508. [PubMed: 9822384]
62. Bruckner G, Seeger G, Brauer K, Hartig W, Kacza J, Bigl V: Cortical areas are revealed by distribution patterns of proteoglycan components and parvalbumin in the Mongolian gerbil and rat. Brain Res 1994;658:67–86. [PubMed: 7834357]
63. Nacher J, Guirado R, Castillo-Gomez E: Structural plasticity of interneurons in the adult brain: role of PSA-NCAM and implications for psychiatric disorders. Neurochem Res 2013;38:1122–1133. [PubMed: 23354722]

64. Gascon E, Vutskits L, Kiss JZ: Polysialic acid-neural cell adhesion molecule in brain plasticity: from synapses to integration of new neurons. Brain Res Rev 2007;56:101–118. [PubMed: 17658613]

65. Gomez-Climent MA, Guirado R, Castillo-Gomez E, Varea E, Gutierrez-Mecinas M, Gilabert-Juan J, Garcia-Mompo C, Vidueira S, Sanchez-Mataredona D, Hernandez S, Blasco-Ibanez JM, Crespo C, Rutishauser U, Schachner M, Nacher J: The polysialylated form of the neural cell adhesion molecule (PSA-NCAM) is expressed in a subpopulation of mature cortical interneurons characterized by reduced structural features and connectivity. Cereb Cortex 2011;21:1028–1041. [PubMed: 20843898]

66. Luke MP, Brown RE, Clarke DB: Polysialylated - neural cell adhesion molecule (PSA-NCAM) promotes recovery of vision after the critical period. Mol Cell Neurosci 2020;107:103527. [PubMed: 32634575]

67. Di Cristo G, Chattopadhyaya B, Kuhlman SJ, Fu Y, Belanger MC, Wu CZ, Rutishauser U, Maffei L, Huang ZJ: Activity-dependent PSA expression regulates inhibitory maturation and onset of critical period plasticity. Nat Neurosci 2007;10:1569–1577. [PubMed: 18026099]

68. Xu D, Hopf C, Reddy R, Cho RW, Guo L, Lanahan A, Petralia RS, Wenthold RJ, O'Brien RJ, Worley P: Narp and NP1 form heterocomplexes that function in developmental and activity-dependent synaptic plasticity. Neuron 2003;39:513–528. [PubMed: 12895424]

69. Swanson A, Willette AA, Alzheimer's Disease Neuroimaging I: Neuronal Pentraxin 2 predicts medial temporal atrophy and memory decline across the Alzheimer's disease spectrum. Brain Behav Immun 2016;58:201–208. [PubMed: 27444967]

70. Wang Z, Jin T, Le Q, Liu C, Wang X, Wang F, Ma L: Retrieval-Driven Hippocampal NPTX2 Plasticity Facilitates the Extinction of Cocaine-Associated Context Memory. Biol Psychiatry 2020;87:979–991. [PubMed: 31836174]

71. Tsui CC, Copeland NG, Gilbert DJ, Jenkins NA, Barnes C, Worley PF: Narp, a novel member of the pentraxin family, promotes neurite outgrowth and is dynamically regulated by neuronal activity. J Neurosci 1996;16:2463–2478. [PubMed: 8786423]

72. Tong L, Shen H, Perreau VM, Balazs R, Cotman CW: Effects of exercise on gene-expression profile in the rat hippocampus. Neurobiol Dis 2001;8:1046–1056. [PubMed: 11741400]

73. Wibrand K, Messaoudi E, Havik B, Steenslid V, Lovlie R, Steen VM, Bramham CR: Identification of genes co-upregulated with Arc during BDNF-induced long-term potentiation in adult rat dentate gyrus in vivo. Eur J Neurosci 2006;23:1501–1511. [PubMed: 16553613]

74. Fuchs EC, Zivkovic AR, Cunningham MO, Middleton S, Lebeau FE, Bannerman DM, Rozov A, Whittington MA, Traub RD, Rawlins JN, Monyer H: Recruitment of parvalbumin-positive interneurons determines hippocampal function and associated behavior. Neuron 2007;53:591–604. [PubMed: 17296559]

75. Van't Spijker HM, Rowlands D, Rossier J, Haenzi B, Fawcett JW, Kwok JCF: Neuronal Pentraxin 2 Binds PNNs and Enhances PNN Formation. Neural Plast 2019;2019:6804575. [PubMed: 31772567]

76. Alves de Alencar Rocha AK, Allison BJ, Yawno T, Polglase GR, Sutherland AE, Malhotra A, Jenkin G, Castillo-Melendez M, Miller SL: Early- versus Late-Onset Fetal Growth Restriction Differentially Affects the Development of the Fetal Sheep Brain. Dev Neurosci 2017;39:141–155. [PubMed: 28273661]

77. Tolcos M, Bateman E, O'Dowd R, Markwick R, Vrijsen K, Rehn A, Rees S: Intrauterine growth restriction affects the maturation of myelin. Exp Neurol 2011;232:53–65. [PubMed: 21867703]

78. Reid MV, Murray KA, Marsh ED, Golden JA, Simmons RA, Grinspan JB: Delayed myelination in an intrauterine growth retardation model is mediated by oxidative stress upregulating bone morphogenetic protein 4. J Neuropathol Exp Neurol 2012;71:640–653. [PubMed: 22710965]

79. Rideau Batista Novais A, Pham H, Van de Looij Y, Bernal M, Mairesse J, Zana-Taieb E, Colella M, Jarreau PH, Pansiot J, Dumont F, Sizonenko S, Gressens P, Charriaut-Marlangue C, Tanter M, Demene C, Vaiman D, Baud O: Transcriptomic regulations in oligodendroglial and microglial cells related to brain damage following fetal growth restriction. Glia 2016;64:2306–2320. [PubMed: 27687291]

80. Gianfranceschi L, Siciliano R, Walls J, Morales B, Kirkwood A, Huang ZJ, Tonegawa S, Maffei L: Visual cortex is rescued from the effects of dark rearing by overexpression of BDNF. Proc Natl Acad Sci U S A 2003;100:12486–12491. [PubMed: 14514885]

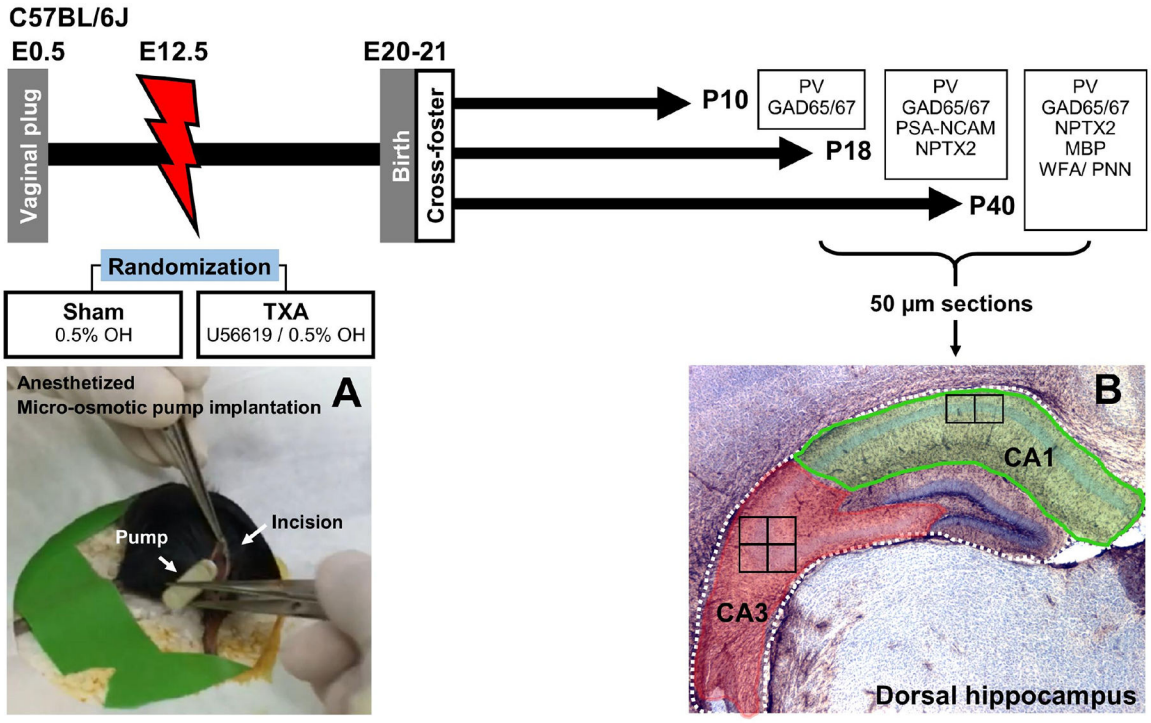

FIGURE 1. Experimental design.

Impregnation of C57BL6/J dams was confirmed by visualizing vaginal plug (E0.5). Under anesthesia micro-osmotic pumps containing either vehicle (0.5% ethanol, OH) were implanted at E12.5 (**A**). Pups were born at P20–21 and were cross-fostered to unmanipulated dams. For these experiments, 3 groups of mice of both sexes were survived to P10 (n=4 per treatment per sex), P18 (n=7 per treatment per sex), or P40 (n=7 per treatment per sex). Following perfusion, brains were collected, post-fixed, cryoprotected, and frozen. Brains were sectioned coronally in a freezing microtome at 50µm. Anterior sections with embedded dorsal hippocampus were used for experiments evaluating target proteins essential for initiation, consolidation, and closure of the CPd of synaptic plasticity in the CA1 and CA3 subfields (**B**). Location of the high magnification fields evaluated are depicted as squares inside the CA1 (x2) and CA3 (x4). **CA**, cornus ammonis; **GAD**, Glutamic acid decarboxylase; **E**, embryonic day; **MBP**, Myelin basic protein; **NPTX2**, neuronal pentraxin 2; **P**, post-natal age; **PNN**, perineural nets; **PSA-NCAM**, polysialylated neural cell adhesion molecule**; PV**, parvalbumin; **TXA**, thromboxane A_2-analog; **WFA**, Wisteria floribunda lectin.

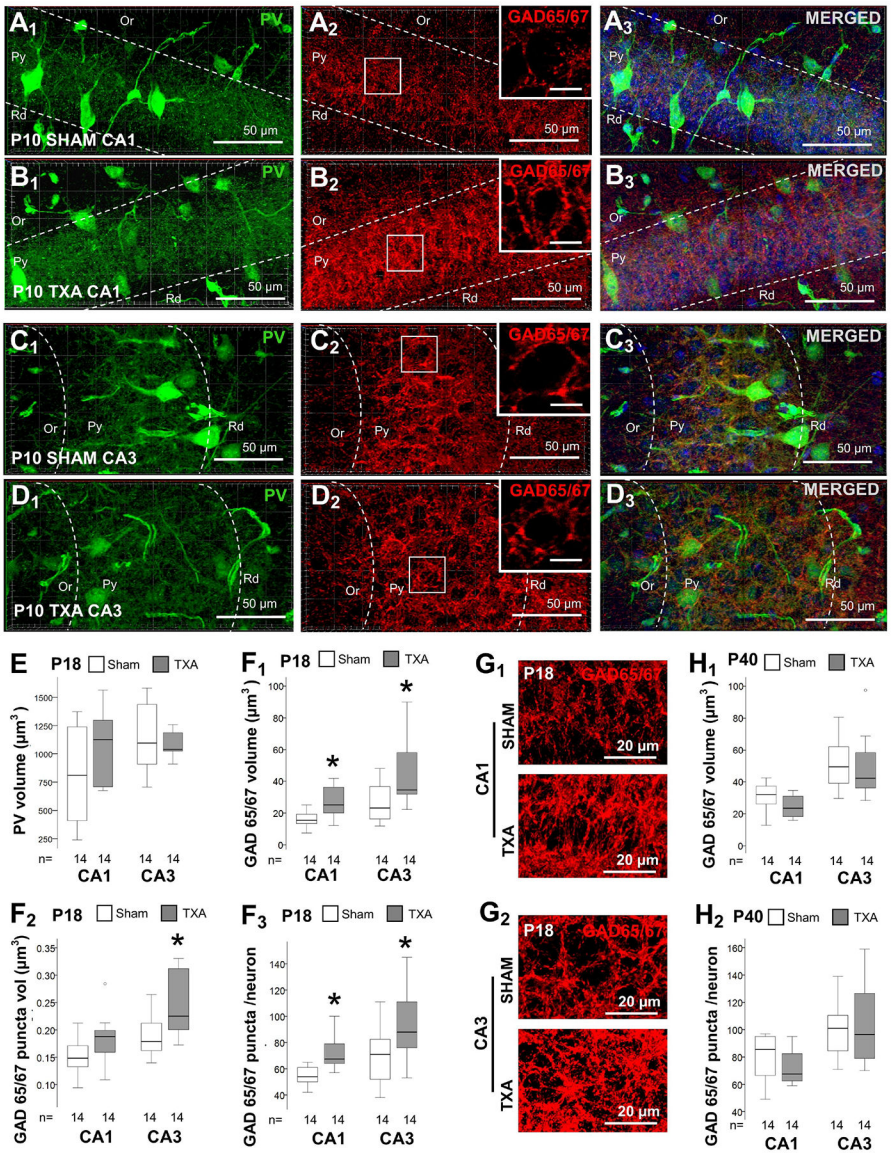

FIGURE 2. Increased GAD 65/67 $^{+}$ synaptic boutons at P18 in the mouse model of IUGR.

Double immunolabeling detected PV IR in green (Alexa 488 goat anti chicken) and GAD 65/67 IR in red (Alexa 568 goat anti rabbit), and DAPI staining in dorsal CA1 (**A** & **B**) and CA3 (**C** & **D**), as shown in panels for P10 sham (**A** & **C**) and IUGR (**B** & **D**) mice. High magnification insets are shown for GAD 65/67 panels ($\mathbf{A}_2$, $\mathbf{B}_2$, $\mathbf{C}_2$, & $\mathbf{D}_2$), with bar representing 10 µm. Box and whiskers plots represent PV total volume (µm^3) at P18 (**E**) and GAD 65/67 at P18 (**F**) and P40 (**H**). Boxes are limited by the 75th and 25th percentiles (interquartile range, IQR) and whiskers are limited by the last data point within 1.5 times the IQR from the median (continuous line inside the box), with outliers represented as °. Mann-Whitney U test was applied to compared experiments groups. *, $p < 0.05$. Unbiased image processing and analysis was performed using Imaris x64 v9.8 software blinded to treatments, sex and time. While no changes were documented in the abundance of PV levels in either CA1 or CA3 at P18, GAD 65/67 total volume (µm^3 per 10^3 µm^3, $\mathbf{F_1}$), volume

per puncta (μm^3, **F_2**), and number of puncta per neuron (**F_3**) were increased in IUGR mice vs. sham. Representative renderings for GAD 65/67 reconstruction from z-stacks using Zen blue software in CA1 (**G_1**) and CA3 (**G_2**). Increase in GAD 65/67 total volume (**H_1**) and number of puncta per neuron (**H_2**) resolved by P40. **CA**, cornus ammonis; **GAD**, Glutamic acid decarboxylase; **Or**, Oriens Layer**; P**, post-natal age; **PV**, parvalbumin; **Py**, pyramidal cell layer; **Rd**, Radiatum layer.

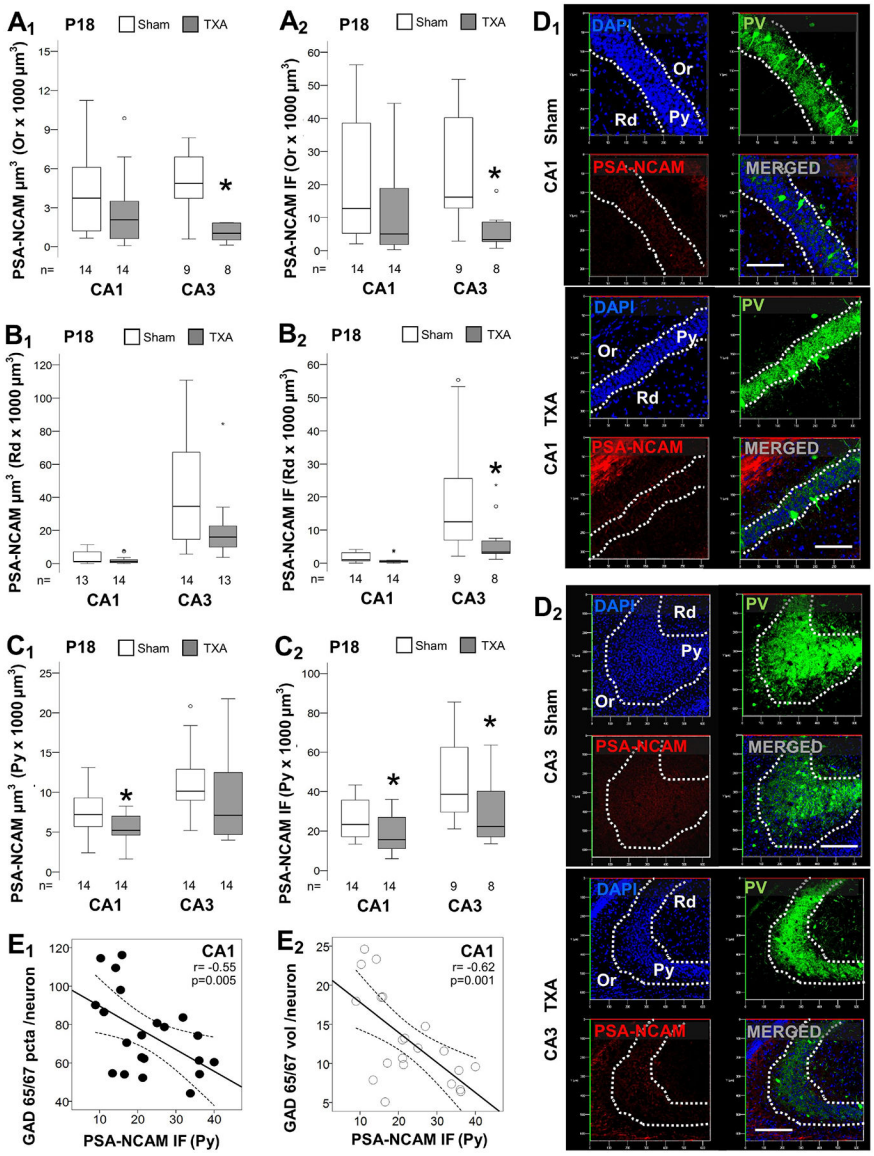

FIGURE 3. Decreased PSA-NCAM in dorsal hippocampus of IUGR mice at P18.

Analysis performed in z-stacks captured from double immunolabeling detecting PV IR in green (Alexa 488 goat anti chicken) and PSA-NCAM IR in red (Alexa 568 goat anti mouse), and DAPI nuclear staining in dorsal hippocampus. Box and whiskers plots represent PSA-NCAM total volume (µm^3 × 10^3 µm^3; **A$_1$**, **B$_1$**, & **C$_1$**) and total IF (A.U. × 10^3 µm^3; **A$_2$**, **B$_2$**, & **C$_2$**) at P18 in CA1 and CA3. Analysis segmented for Or (**A**), Rd (**B**), and Py (**C**) layers of the dorsal CA1 and CA3. Boxes are limited by the 75th and 25th percentiles (interquartile range, IQR) and whiskers are limited by the last data point within 1.5 times the IQR from the median (continuous line inside the box), with outliers represented as °. Mann-Whitney U test was applied to compared experimental groups. *, $p < 0.05$. Unbiased image processing and analysis was performed using Imaris x64 v9.8 software blinded to treatments, sex and time. Representative reconstruction renderings from z-stacks using Zen blue software in CA1 (**D$_1$**) and CA3 (**D$_2$**) are shown. The decrease in PSA-NCAM

IR (*x*-axis) inversely correlated with the increase in GAD 65/67 puncta per neuron ($\mathbf{E_1}$) and volume per neuron ($\mathbf{E_2}$) at P18. Continuous line represents the fitted line derived from a linear regression and the discontinuous line represent the 95% CI. Spearman Rho correlation was applied. **A.U**., arbitrary units; **CA**, cornus ammonis; **GAD**, Glutamic acid decarboxylase; **IF**, immunofluorescence; **Or**, Oriens Layer**; P**, post-natal age; **pcta**, puncta; **PV**, parvalbumin; **Py**, pyramidal cell layer; **r**, Rho coefficient; **Rd**, Radiatum layer.

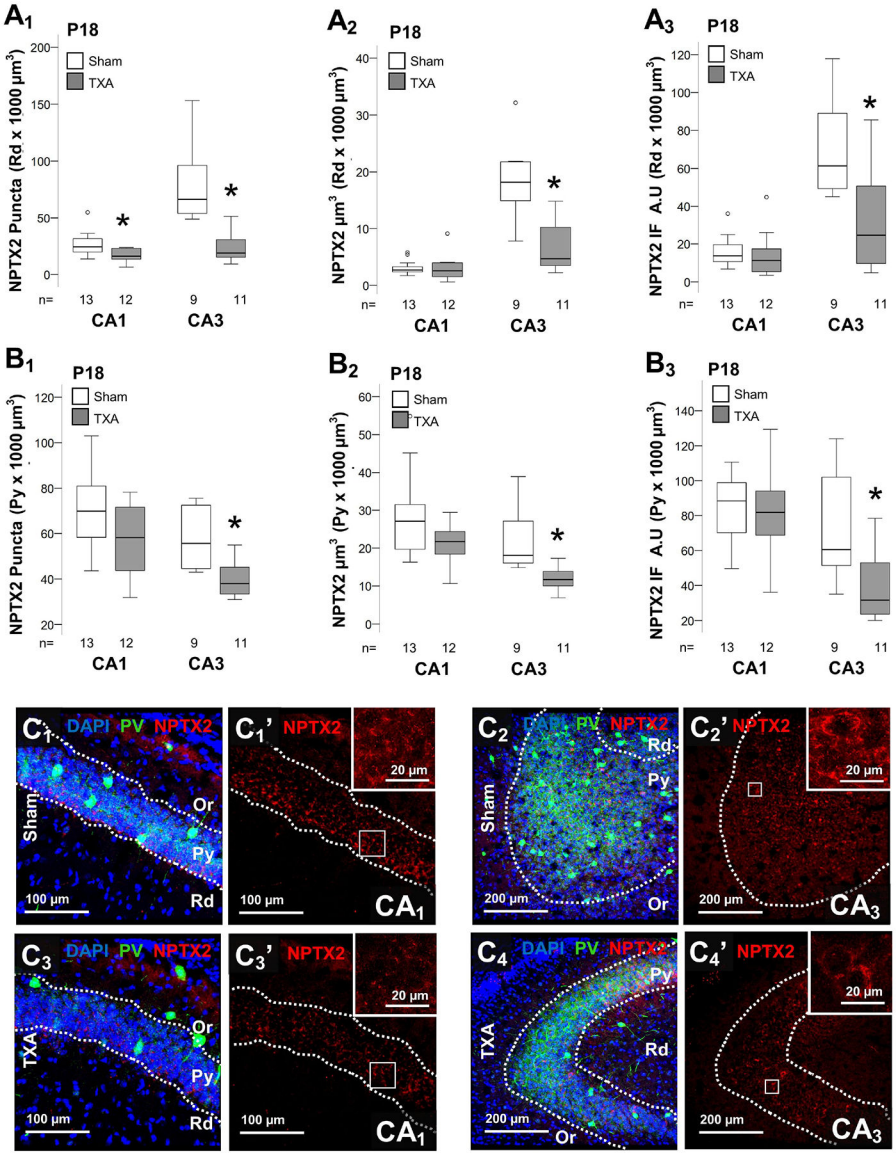

Figure 4. Decrease NPTX2 levels in the CA3 in IUGR mice at P18.

Analysis performed in z-stacks captured from double immunolabeling detecting PV IR in green (Alexa 488 goat anti chicken) and NPTX2 IR in red (Alexa 568 goat anti rabbit), and DAPI nuclear staining in dorsal hippocampus. Box and whiskers plots represent NPTX2 number of puncta per 10^3 µm^3 (**A_1** & **B_1**), total volume (µm^3 × 10^3 µm^3; **A_2**& **B_2**) and total IF (A.U. × 10^3 µm^3; **A_3** & **B_3**) at P18 in CA1 and CA3. Analysis segmented for Rd (**A**), and Py (**B**) layers of the dorsal CA1 and CA3. Boxes are limited by the 75th and 25th percentiles (interquartile range, IQR) and whiskers are limited by the last data point within 1.5 times the IQR from the median (continuous line inside the box), with outliers represented as °. Mann-Whitney U test was applied to compared experimental groups. *, $p < 0.05$. Unbiased image processing and analysis was performed using Imaris x64 v9.8 software blinded to treatments, sex and time. Representative reconstruction renderings from z-stacks using Zen blue software in CA1 (**C_1** & **C_3**) and CA3 (**C_2** & **C_4**). **A.U**., arbitrary units; **CA**, cornus

ammonis; **IF**, immunofluorescence; **Or**, Oriens Layer**; P**, post-natal age; **pcta**, puncta; **PV**, parvalbumin; **Py**, pyramidal cell layer; **Rd**, Radiatum layer.

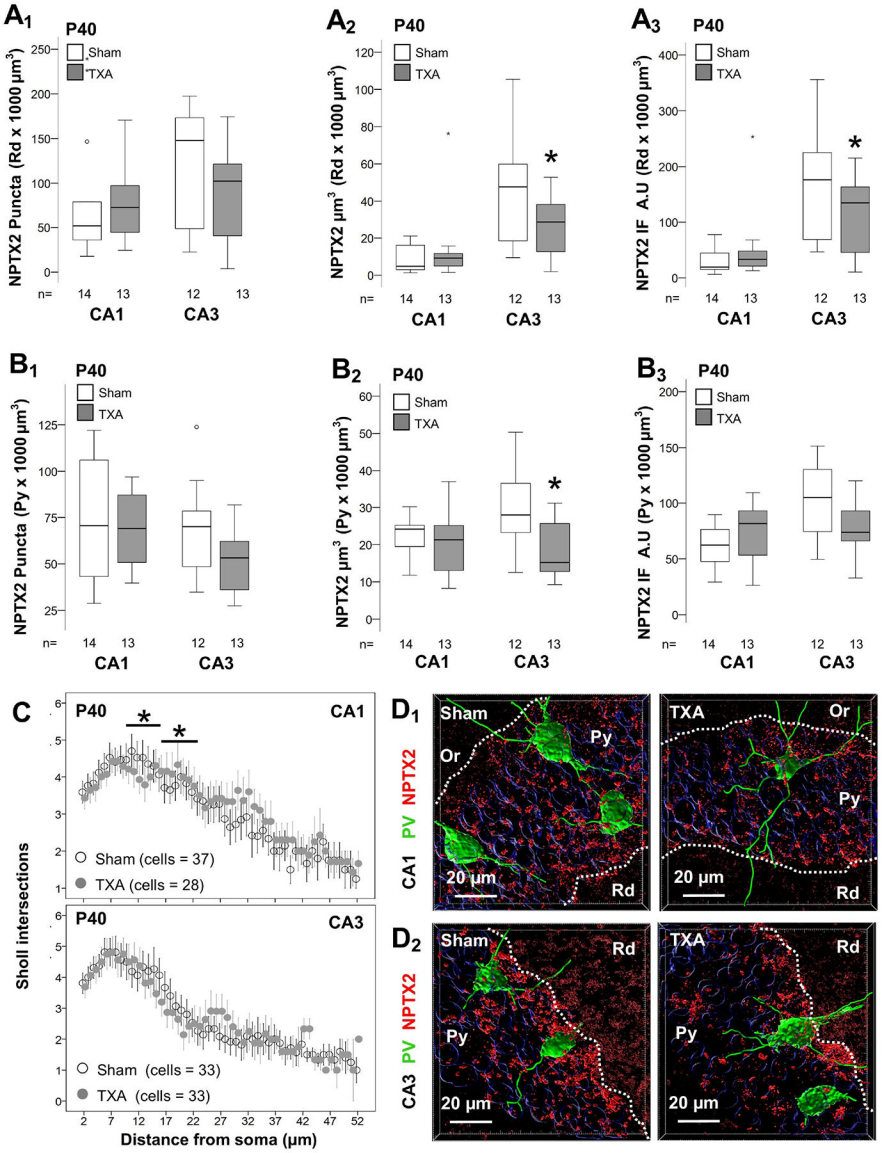

Figure 5. Persistent decrease NPTX2 levels in the CA3 in IUGR mice at P40 with minimal dendritic alteration of PV $^{+}$ INs.

Analysis performed in z-stacks captured from double immunolabeling detecting PV IR in green (Alexa 488 goat anti chicken) and NPTX2 IR in red (Alexa 568 goat anti rabbit), and DAPI nuclear staining in dorsal hippocampus. Box and whiskers plots represent NPTX2 number of puncta per 10^3 µm^3 (**A$_1$** & **B$_1$**), total volume (µm^3 × 10^3 µm^3; **A$_2$**& **B$_2$**) and total IF (A.U. × 10^3 µm^3; **A$_3$** & **B$_3$**) at P18 in CA1 and CA3. Analysis segmented for Rd (**A**), and Py (**B**) layers of the dorsal CA1 and CA3. Boxes are limited by the 75th and 25th percentiles (interquartile range, IQR) and whiskers are limited by the last data point within 1.5 times the IQR from the median (continuous line inside the box), with outliers represented as °. Mann-Whitney U test was applied to compared experimental groups. *, $p < 0.05$. Unbiased image processing and analysis was performed using Imaris x64 v9.8 software blinded to treatments, sex and time. Distribution of the number of Sholl intersections (mean ± SEM, *y*-axis) counted away from the soma of PV $^{+}$ INs (*x*-axis)

suggested modest differences between treatment groups at P40 (**C**). Representative surface reconstruction renderings from z-stacks using Imaris x64 v9.8 software in CA1 (**D_1**) and CA3 (**D_2**), showing reconstructed NPTX2 puncta (red channel) and PV $^+$ INs (green channel). **A.U**., arbitrary units; **CA**, cornus ammonis; **IF**, immunofluorescence; **Or**, Oriens Layer**; P**, post-natal age; **PV**, parvalbumin; **Py**, pyramidal cell layer; **Rd**, Radiatum layer.

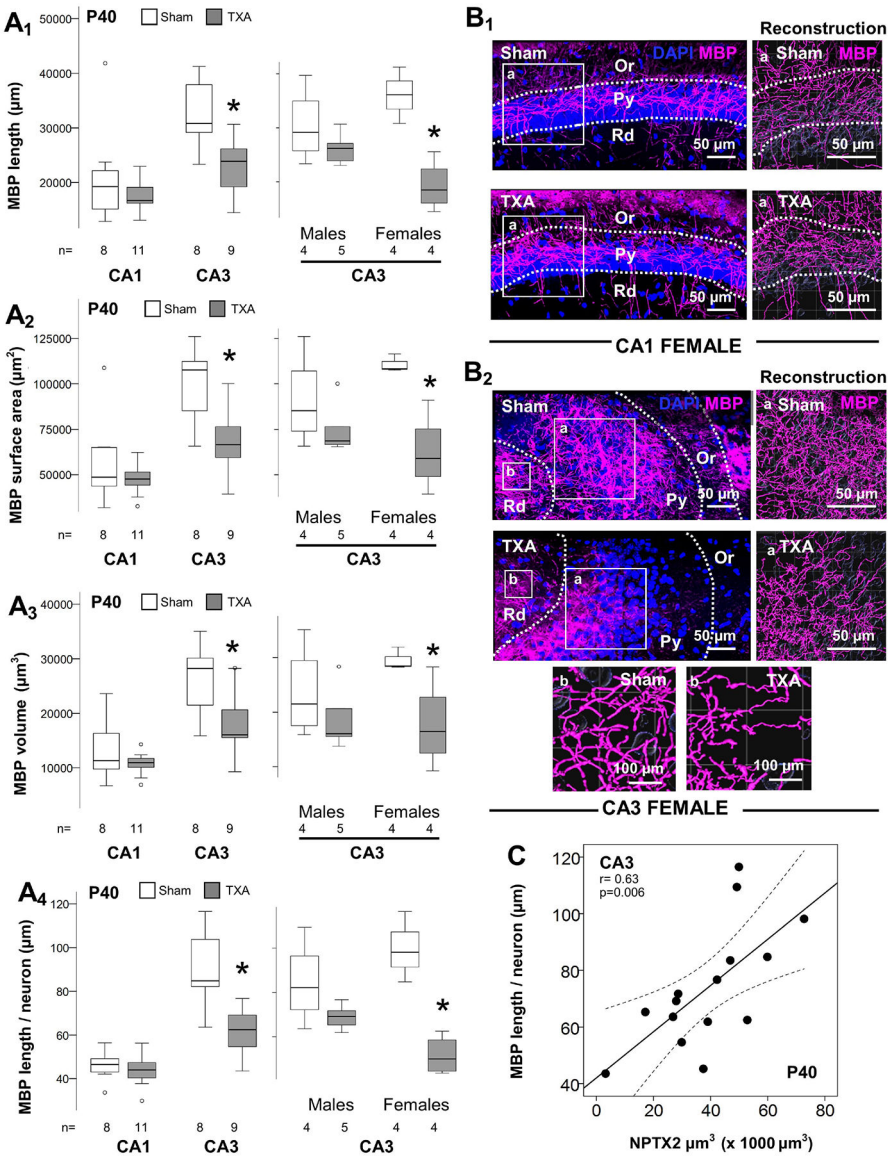

Figure 6. Sexual dysmorphism in disruption of myelination in the CA3 of IUGR mice at P40.

Analysis performed in z-stacks captured from immunolabeling detecting MBP IR in magenta (Alexa 647 goat anti mouse) and DAPI nuclear staining in dorsal hippocampus. Box and whiskers plots represent filament analysis using Imaris software for MBP-stained myelinated axons in the CA1 and CA3, and stratification by sex of CA3 analysis. Analysis included total filament length (µm, **A_1**), surface area (µm^2, **A_2**), and volume (µm^3, **A_3**) as well as filament length per neuron (µm, **A_4**). Boxes are limited by the 75th and 25th percentiles (interquartile range, IQR) and whiskers are limited by the last data point within 1.5 times the IQR from the median (continuous line inside the box), with outliers represented as °. Mann-Whitney U test was applied to compared experimental groups. *, $p < 0.05$. Unbiased image processing and analysis was performed using Imaris x64 v9.8 software blinded to treatments, sex and time. Representative rendering of z-stacks produced using ZenBlue software for CA1 (**B_1**) and CA3 (**B_2**) of sham and IUGR female mice are

shown, with high magnification panels of reconstruction of myelinated MBP $^{+}$ axons (**a**). A second set of high magnification panels localized in the Rd are also shown for CA3 (**b**). MBP $^{+}$ filament length (μm; *y*-axis) directly correlated with deficits in NPTX2 volume (μm^3; *x*-axis) at P40 in the CA3. Continuous line represent the fitted line derived from a linear regression and the discontinuous line represent the 95% CI. Spearman Rho correlation was applied. **CA**, cornus ammonis; **Or**, Oriens Layer**; P**, post-natal age; **MBP**, Myelin basic protein; **Py**, pyramidal cell layer; **r**, Rho coefficient; **Rd**, Radiatum layer.

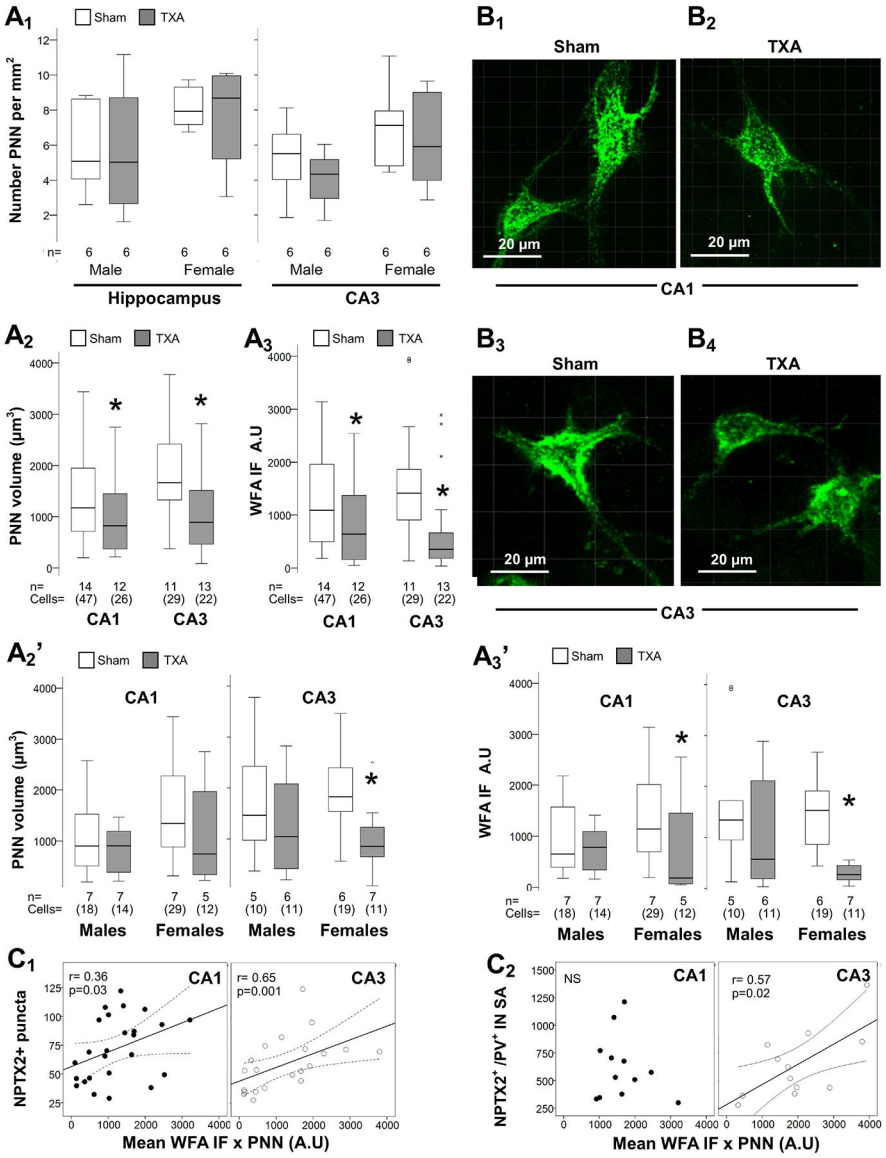

Figure 7. Disturbed PNN formation in the dorsal hippocampus of IUGR mice at P40.

Analysis performed in z-stacks captured from fluorescein conjugated WFA staining detecting PNN in green channel in dorsal hippocampus. Box and whiskers plots represent PNN number per mm^2 in the dorsal hippocampus and the CA3 stratified by sex (**A_1**), total volume (in $\mu m^3 \times 10^3$ μm^3; **A_2**) and total WFA IF (A.U. $\times 10^3$ μm^3; **A_3**) at P40 in CA1 and CA3. Sexual dimorphism for total PNN volume (**A_2**') and WFA IF (**A_3**') are also shown. Boxes are limited by the 75th and 25th percentiles (interquartile range, IQR) and whiskers are limited by the last data point within 1.5 times the IQR from the median (continuous line inside the box). Mann-Whitney U test was applied to compared experimental groups. *, $p < 0.05$. Unbiased image processing and analysis was performed using Imaris x64 v9.8 software blinded to treatments, sex and time.

Representative surface reconstruction renderings from z-stacks using Zen blue software in CA1 (**B_1 – B_2**) and CA3 (**B_3 – B_4**), showing reconstructed PNNs (green channel).

Videos capturing 3D-reconstructions are available on-line (Supplemental material). Number of $NPTX2^+$ puncta per 10^3 μm^3 (**C_1**) and number of $NPTX2^+$ puncta per 10^2 μm of PV IN surface area (**C_2**) (*y*-axis), both directly correlated with WFA IF per PNN (*x*-axis) at P40 in the CA1 and CA3. Continuous line represents the fitted line derived from a linear regression and the discontinuous line represent the 95% CI. Spearman Rho correlation was applied. **A.U**., arbitrary units; **CA**, cornus ammonis; **IF**, immunofluorescence; **NPTX2**, neuronal pentraxin 2; **P**, post-natal age; **PNN**, perineural nets; **PV**, parvalbumin; **SA**, surface area; **TXA**, thromboxane A_2-analog; **WFA**, Wisteria floribunda lectin.

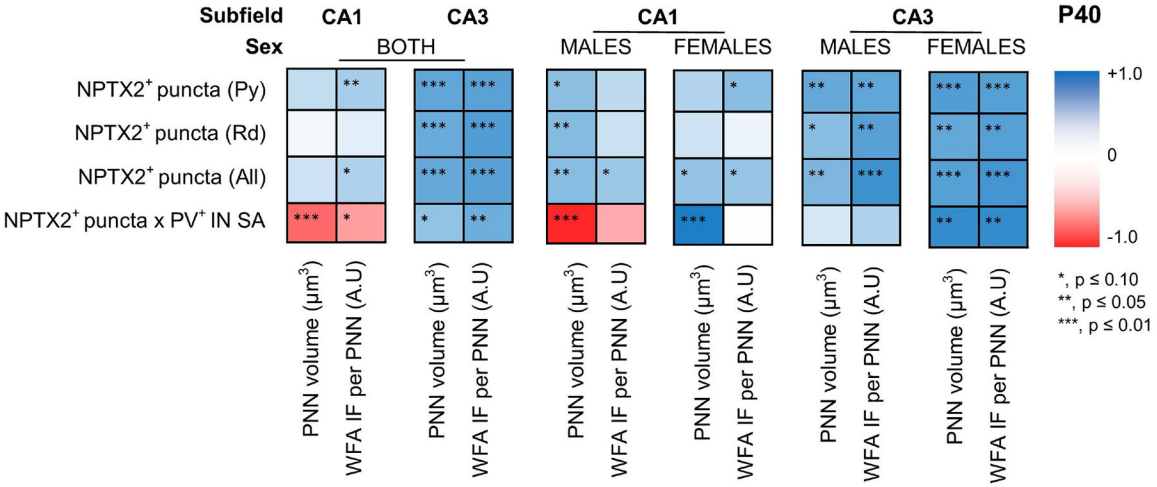

FIGURE 8. Heatmap representing the strength of Spearman Rho correlation between NPTX2$^+$ puncta and PNN disruption at P40.

Intensity of blue or red boxes represent the extremes of the Rho (ρ) coefficient of +1.0 to −1.0, respectively, as showed in grading bar on the right. *, $p \leq 0.10$; **, $p \leq 0.05$; ***, $p \leq 0.01$. Sexual dimorphism shown in the relationship of PNN volume vs. number of NPTX2$^+$ puncta per 10^2 µm of PV IN surface area in the CA1. **CA**, cornus ammonis; **IF**, immunofluorescence; **NPTX2**, neuronal pentraxin 2; **P**, post-natal age; **PNN**, perineural nets; **PV**, parvalbumin; **SA**, surface area; **WFA**, Wisteria floribunda lectin.